Journal of Materials Chemistry A

Materials for energy and sustainability

www.rsc.org/MaterialsA

Volume 1 | Number 43 | 21 November 2013 | Pages 13365–13688

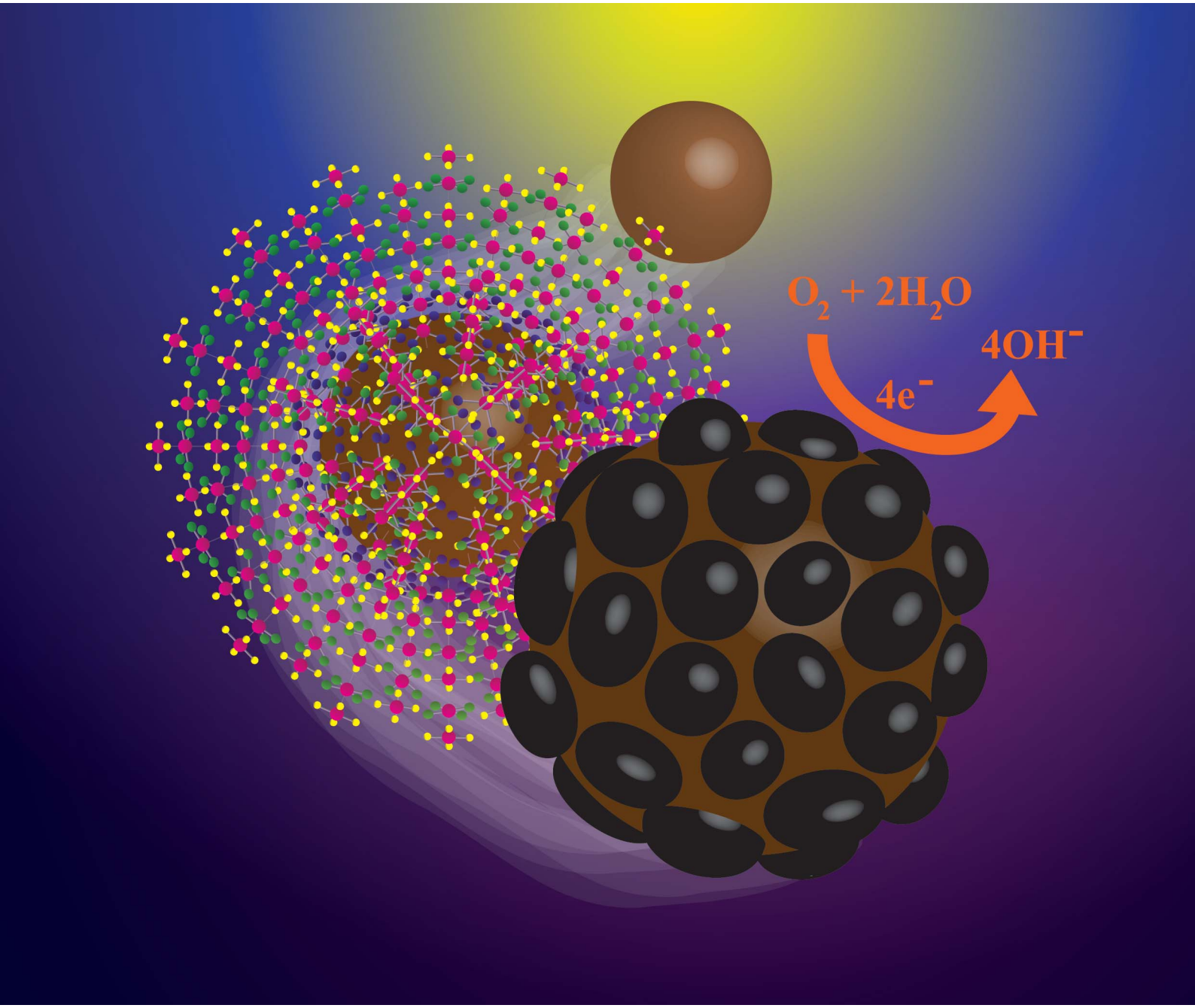

ISSN 2050-7488

RSC Publishing

PAPER

Donald A. Robinson and Keith J. Stevenson

Uniform epitaxial growth of Pt on Fe_3O_4 nanoparticles; synergetic enhancement to Pt activity for the oxygen reduction reaction

2050-7488(2013)1:43;1-S

Journal of Materials Chemistry A

RSC Publishing

PAPER

View Article Online
View Journal | View Issue

Cite this: J. Mater. Chem. A, 2013, 1, 13443

Uniform epitaxial growth of Pt on Fe_3O_4 nanoparticles; synergetic enhancement to Pt activity for the oxygen reduction reaction†

Donald A. Robinson and Keith J. Stevenson*

Received 31st July 2013
Accepted 28th August 2013

DOI: 10.1039/c3ta12987j

www.rsc.org/MaterialsA

A synthetic strategy for achieving uniform shell-like epitaxial growth of Pt on Fe_3O_4 nanoparticles is introduced. The method involves the controlled high-density loading of Pt^{2+} by the linear growth of repeatedly stacked units of $[Pt(NH_2OH)_4]^{2+}$ and $[PtCl_4]^{2-}$, followed by a subsequent reduction step. In comparison to commercial Pt-based fuel cell catalysts, the resulting Pt–Fe_3O_4 hybrid nanostructures were found to exhibit improved Pt specific activity for the electroreduction of oxygen in alkaline media, which is attributed to charge transfer from Fe_3O_4 to Pt. The Pt shell-type structure of the Pt–Fe_3O_4 hybrids was found to protect the Fe_3O_4 cores from corrosion, thus ensuring catalyst stability. A uniform Pt coating was also deposited evenly over SiO_2 microspheres using this method, thus demonstrating its potential as a general strategy for platinum deposition on essentially any amine-functionalized surface.

Introduction

Recent developments in the synthesis of inorganic colloids have brought about the investigation of a new class of functional material, known as hybrid nanostructures (HNs),[1] which consist of a combination of two or more materials of different composition into a single integrated nanosized structure by solid–solid heterojunctions. Characterization of HNs often reveals evidence of synergetic behavior, which arises if the domains of the component materials are confined to the nanoscale so that they influence the properties of one another. In contrast to an integrated system of bulk materials whereby synergetic properties are limited to interfacial regions, cooperative effects are notably more significant in HNs since interfacial contacts are maximized with respect to the bulk.[1a,2]

Synergetic effects have proven influential in modifying the electrocatalytic activity of HNs towards heterogeneous fuel cell reactions, particularly in the case of metal/metal oxide HNs.[3] In early investigations, interactions of metals with metal oxide supports were considered to be negligible until Tauster and coworkers introduced the concept of strong metal–support interactions (SMSI),[4] pertaining to how different metal oxide supports influence chemisorption of CO and H_2 onto noble metal nanoparticles. Since then, several articles have reported modification to the activity of catalytic metal domains by interactions with different bulk or nanostructured metal oxide supports, *e.g.* RuO_2,[5] CeO_2,[6] SiO_2,[7] TiO_2,[3a–c,8] NbO_x,[3d,e,9] WO_3,[3f,g,10] MnO_x,[3h,i,11] γ-Fe_2O_3,[3j] and Fe_3O_4.[3k,12]

A particularly substantial synergetic enhancement to the electrocatalytic oxygen reduction reaction (ORR) activity on platinum was reported by Sun and coworkers for monodispersed heterodimers composed of magnetite (Fe_3O_4) and platinum nanodomains.[3k] The catalytic improvement is attributed to a charge transfer from the magnetite domain to the platinum, as evidenced by X-ray photoelectron spectroscopy (XPS). The major disadvantage of these heterostructures with regard to catalysis is stability. The majority of Fe_3O_4 surfaces on Pt–Fe_3O_4 dimers are exposed to oxygen and therefore prone to irreversibly oxidize to the thermodynamically favored Fe_2O_3 species in aerobic environments.[13] The stability of Fe_3O_4 is further compromised if the material is exposed to common fuel cell pH conditions, since dissolution of Fe_3O_4 occurs in both strongly acidic[14] and alkaline[15] media. A more recent study found that ~9 nm Fe_3O_4 nanoparticles in pH 12–13 aqueous suspension completely oxidize after about 3 months at room temperature.[16]

We propose that platinum–magnetite hybrid nanostructures (Pt–MHNs) based on a core–shell type design are more suitable for catalytic stability. Our rationale is that Pt coatings serve to protect the underlying Fe_3O_4 cores from reactive adsorbates and thus improve stability. The methods described herein are aimed at synthesizing such nanostructures without the use of long-chain organic capping ligands or polymers which passivate the Pt surface.[17] Instead, our method relies on a unique form of controlled platinum deposition on amine-terminated nanoparticles (AT-MNPs), which involves the epitaxial growth of platinous backbone-polymerized complexes (PtBPCs) and their subsequent reduction to form Pt–MHNs with high Pt surface

Department of Chemistry, University of Texas at Austin, Austin, Texas 78712, USA; Web: stevenson@cm.utexas.edu; Fax: +1 512 471 8696; Tel: +1 512 471 3127

† Electronic supplementary information (ESI) available: Elemental analysis from FAA and EDX, STEM images, EDX spectra, TGA, and voltammetry. See DOI: 10.1039/c3ta12987j

coverage. Thorough characterization is provided for both the resulting Pt–MHNs and the PtBPC–MHN intermediate structures. An evaluation on the electrocatalytic activity and stability of Pt–MHNs is presented along with direct experimental comparisons to Pt–Fe_3O_4 heterodimers and commercial Pt fuel cell nanocatalysts. Moreover, when amine-terminated SiO_2 microspheres are used as an alternative substrate to AT-MNPs, platinum–silica hybrid microstructures (Pt–SiHMs) are achieved. We therefore propose that the Pt coating method can be applied to virtually any amine-functionalized surface.

Experimental

Chemicals

Potassium tetrachloroplatinate (K_2PtCl_4, 99.9%), iron(III) chloride hexahydrate ($FeCl_3 \cdot 6H_2O$, 97%), iron(0) pentacarbonyl ($Fe(CO)_5$, 99.999%), 3-aminopropyltriethoxysilane (APTES, 99%), tetraethylorthosilicate (TEOS, 98%), and chloroform were obtained from Sigma-Aldrich. Hydroxylamine hydrochloride ($NH_2OH \cdot HCl$, ACS grade), anhydrous potassium acetate (KAc, ACS grade), sodium citrate dihydrate (ACS grade), sodium hydroxide (ACS grade), ammonium hydroxide (NH_4OH, 30%, ACS grade), and ethylene glycol (EG, ACS grade) were purchased from Fisher Scientific. Absolute ethanol (ACS grade) was obtained from Pharmco-Aaper. Sodium borohydride ($NaBH_4$, 98%), 1,6-hexanediamine ($NH_2C_6H_{12}NH_2$, 99.5%), oleic acid (97%), oleylamine (C18 content 80–90%), and platinum acetylacetonate ($Pt(acac)_2$, 98%) were purchased from Acros Organics. Carbon black (Vulcan XC72) was obtained from Cabot Corp. All water was purified to 18.2 MΩ cm using a Barnstead Epure System. All chemicals were used as received.

Synthesis of AT-MNPs

The synthesis of AT-MNPs was followed according to the method of Wang *et al.*,[18] with some modifications. A solution of $NH_2C_6H_{12}NH_2$ (2.2 g), KAc (0.78 g) and $FeCl_3 \cdot 6H_2O$ (0.33 g) in EG (10 mL) was transferred into a Teflon-lined autoclave and reacted at 180 °C for 5 h. The precipitated AT-MNP product was then rinsed with ethanol and water (3 times each).

Synthesis of PtBPC–MHNs

AT-MNP (10 mg) was mixed with 160 mL water in a 250 mL round-bottom flask. The mixture was agitated into suspension by sonication for 15 min. in a 60 °C sonication bath. A 20 mL aqueous solution containing 140 mg sodium citrate and a certain concentration of K_2PtCl_4 was then added. After 30 min of sonication, a solution of $H_2NOH \cdot HCl$ (70 mg) in 20 mL of 50 mM sodium phosphate buffer (pH 7) was added. After 2 h the PtBPC–MHN product was isolated by centrifuge and rinsed once with 0.010 M NaOH followed by 3 washings with water, using a permanent magnet to collect PtBPC–MHNs between rinses. Four separate syntheses with varied initial concentrations of K_2PtCl_4 (0.125 mM, 0.250 mM, 0.375 mM, and 0.500 mM) led to different PtBPC–MHN products varying in Pt : Fe atomic ratio. A control synthesis was carried out using the same procedure as described above except without $H_2NOH \cdot HCl$.

Synthesis of Pt–MHNs by wet chemical reduction

A 5 mg portion of PtBPC–MHNs and 60 mg sodium citrate were sonicated in 30 mL water for 10 min. A solution containing $NaBH_4$ (20 mg) in 10 mL water was then added and the mixture was sonicated for 1 h. Pt–MHN product was magnetically isolated and washed with water 3 times.

Preparation of Pt–MHN/C by thermally driven reduction

A PtBPC–MHN suspension (8 mg in 8 mL of ethanol–water 1/1 v/v) was mixed with a suspension of Vulcan XC72 (32 mg in 32 mL of ethanol–water 1/1 v/v) and sonicated for 1 h. The final mixture was then dried by rotary evaporation and heated under air at 190 °C or 240 °C for 5 h. A 10 mg portion of the sample that was annealed in air at 240 °C was reacted with $NaBH_4$ (20 mg) in 50 mL ethanol–water 1/1 v/v for 1 h under sonication. The Pt–MHN/C product was rinsed 3 times with 1/1 v/v ethanol–water.

Synthesis of Pt–Fe_3O_4 heterodimers

Pt–Fe_3O_4 heterodimers were synthesized following the procedure described by Wang *et al.*,[3k] with some slight modifications. First, 5 nm Pt seeds were prepared according to the literature.[19] For the synthesis of 5–17 nm Pt–Fe_3O_4 dimer nanoparticles, 1-octadecene (20 mL) and oleic acid (1 mL) were mixed and degassed by Schlenk line techniques using N_2 gas, then heated to 120 °C. Under a N_2 blanket, $Fe(CO)_5$ (0.14 mL, 1 mmol) was added. After 10 min, oleylamine (1 mL) was added followed by 3 nm Pt seeds (20 mg, 2 mL hexane dispersion in 10 mg mL^{-1}). The solution was heated to 300 °C and kept at this temperature for 20 min before cooling down to room temperature. The product was precipitated by ethanol and isolated by centrifugation. Pt–Fe_3O_4 NPs were purified by 3 repeated cycles of dispersing in hexane, precipitating with ethanol, and centrifugation. A 10 mg portion of the purified Pt–Fe_3O_4 NPs was mixed with 40 mg of Vulcan XC72 in 10 mL of chloroform and sonicated for 1 h. The sample was dried by rotary evaporation and annealed at 185 °C for 5 h.

Synthesis of PtBPC–SiHMs and Pt–SiHMs

Silicon dioxide microparticles with diameter of 2.0 (±0.1) μm were obtained from Polysciences, Inc. The product was purified by repeated dispersing in ethanol and isolation by centrifugation, discarding the supernatant after each centrifuge cycle. For amine functionalization,[20] a 0.10 mL portion of 30% NH_4OH(aq.) was added to 10 mL of a 1 mg mL^{-1} suspension of silica nanoparticles under rapid stirring, followed by the addition of 0.50 mL of a 10% v/v solution of APTES in ethanol. The mixture was stirred rapidly for 24 h. The same procedure carried out above for the synthesis of PtBPC–MHNs was applied for PtBPC–SiHMs, using 100 mg of amine-functionalized silica particles instead of 10 mg AT-MNPs and a 0.375 mM solution of K_2PtCl_4. The product was isolated by centrifugation. Reduction was carried out by adding a solution containing 20 mg of $NaBH_4$ in 10 mL water to a suspension of PtBPC–SiHMs (10 mg) and sodium citrate (60 mg) in 30 mL water, followed by sonication for 1 h. Product was isolated and rinsed repeatedly by centrifugation.

Nanoparticle characterization

Scanning transmission electron microscopy (STEM) and energy dispersive X-ray spectroscopy (EDX) were performed using a Hitachi-S5500 microscope operated at 30 kV equipped with a Bruker Quantax 4010 EDX detector. High resolution imaging was carried out with an FEI TECNAI G2 F20 X-TWIN transmission electron microscope (TEM). Samples were prepared for electron microscopy by dropping nanoparticle suspensions onto Formvar-coated TEM grids and drying at 50 °C. Powder X-ray diffraction (XRD) was performed on a Rigaku R-axis Spider diffractometer using Cu Kα radiation. A Mettler-Toledo TGA/DSC was used for thermogravimetric analysis (TGA). The air flow was maintained at 60 mL min^{-1}. Initially, the sample was held at 110 °C for 10 min to evaporate any residual solvents. The samples (~2 mg each) were than heated to 900 °C at a rate of 20 °C min^{-1}. The final mass% remaining was used to calculate the metal loading on electrodes used in electrocatalysis experiments. Elemental analysis was conducted using a GBC 908AA flame atomic absorption (FAA) spectrometer equipped with Pt and Fe source lamps. Samples for FAA were prepared by digesting PtBPC–MHNs in aqua regia and diluting to the proper concentrations. X-ray photoelectron spectroscopy (XPS) was performed on a Physical Electronics PHI 5700 equipped with a dual anode source operating on the Mg filament (1253.6 eV). All high-resolution peak positions were calibrated to C-1s at 284.5 eV and peak areas were calculated using a standard Gaussian/Lorentzian fit with a Shirley background correction.

Reagents and instruments for electrocatalysis studies

Potassium hydroxide (KOH, ACS grade, Fisher Sci.), perchloric acid ($HClO_4$, ACS grade, Fisher Sci.), and Nafion® solution (5 wt% in lower aliphatic alcohols–H_2O mix, Sigma-Aldrich) were used as purchased without further purification. Commercial platinum fuel cell catalyst (Pt/C, 20 wt% Pt on carbon black, ETEK) was thermally activated under reducing atmosphere before use. The Pt/C catalyst powder was placed into a quartz tube furnace, which was subsequently purged with forming gas. The temperature was ramped to 350 °C over the course of 2 h under gas flow and was kept at this temperature for an additional 2 h. Catalyst inks[21] were prepared by sonicating 2 mg of carbon-supported catalyst powder in 2 mL 0.05 wt% Nafion solution in ethanol for 30 min. The catalyst ink (10 μL) was dropcast onto a glassy carbon rotating disk electrode (GCRDE, 5 mm diameter, Pine Instruments) and allowed to dry slowly under a glass vial, forming a thin film containing 10 μg of catalyst.

Electrochemical measurements were performed using a Metrohm Autolab PGSAT302N potentiostat equipped with high speed rotator (Pine Instruments). A gold wire and $Hg/HgSO_4$ (sat. K_2SO_4, CH Instruments) electrodes were used as the counter and reference electrodes, respectively. Catalyst films on GCRDEs were used as the working electrodes. ORR experiments were performed in O_2-saturated 0.10 M KOH solutions using an RDE setup with a high speed rotator from Pine Instruments. The 0.10 M KOH solution was bubbled with O_2 for at least 10 min before linear sweep voltammograms (LSVs) were recorded as cathodic sweeps at 5 mV s^{-1} scan rate and 1600 rpm rotation. Electrochemically active surface area (ECSA) analysis was performed using argon-purged 0.10 M $HClO_4$ solution as the electrolyte. ECSA values were calculated from charge based on integration of the H desorption peak currents (with respect to time) from cyclic voltammograms acquired at 0.1 V s^{-1}.[22] Kinetic currents, calculated from the LSVs using the Koutecky–Levich equation,[23] were normalized to Pt ECSA and Pt mass loadings (determined by TGA and FAA) to report specific activity and mass activity, respectively. All potentials are reported *vs.* the regular hydrogen electrode (RHE) in 0.10 M KOH, which is shifted +1.417 V *vs.* the $Hg/HgSO_4$ reference ($Hg/HgSO_4$ (sat. K_2SO_4) + 0.65 V = NHE; NHE + 0.059 × pH = RHE).

Results and discussion

The aqueous synthesis of Pt–MHNs is outlined as a two-step method in Scheme 1. Synthesis of Pt–MHNs begins with amine-terminated magnetite nanoparticles (AT-MNPs) sized at 27 (±5) nm, which were prepared following the procedure reported by Li and coworkers.[18] The method employs 1,6-hexanediamine ($NH_2C_6H_{12}NH_2$) as both stabilizing ligand and amine functionalizing agent. The amine functional groups serve as sites for Pt^{2+} ion chemisorption and amine complex formation upon the addition of K_2PtCl_4 in water, as shown in step 1 of Scheme 1. The introduction of hydroxylamine (NH_2OH) under sonication and heating then promotes polymeric growth of $([Pt(NH_2OH)_4][PtCl_4])_n$. The epitaxial growth process for these so-called platinous backbone-polymerized complexes (PtBPCs) initiates at $[Pt(NH_2C_6H_{12}NH_2)_n]^x$ seed complexes adsorbed on the Fe_3O_4 surface. Further growth and evolution of the PtBPCs eventually leads to the formation of an encapsulating outer layer. It is important to note that the role of NH_2OH in step 1 is not to serve as a reducing agent, as previously reported for coating Au on Fe_3O_4 nanoparticles,[24] but to promote PtBPC encapsulation.

We propose that the PtBPC structures resemble the primary units that make up Magnus' salts[25] and their derivatives,[26] which have the general composition $[Pt(NH_2R)_4][PtCl_4]$. The tetragonal

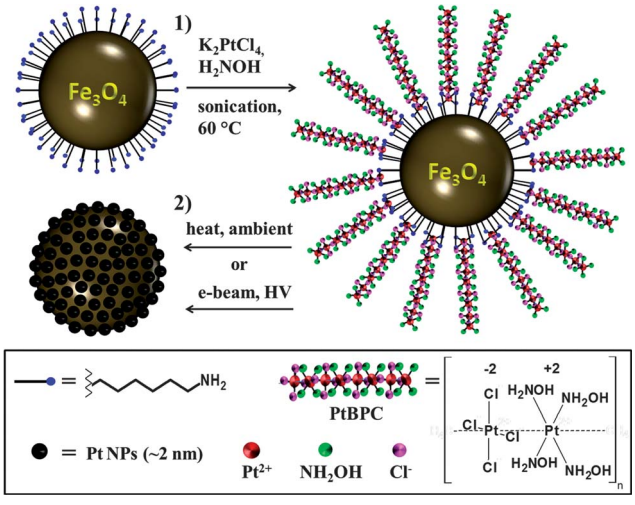

Scheme 1 Synthesis and proposed general structure of PtBPC–MHN and Pt–MHN.

single crystal of $[Pt(NH_2R)_4][PtCl_4]$ is constructed from linear arrays formed by alternately stacked $[Pt(NH_2R)_4]^{2+}$ and $[PtCl_4]^{2-}$ planar complexes with weak Pt–Pt intermolecular bonds and electrostatic interactions.[26,27] Magnus' salts and their NH_2OH derivatives, $[Pt(NH_2OH)_4][PtCl_4]$,[28] are poorly soluble in water and easily isolated as precipitates.[25] The PtBPC–magnetite hybrid nanostructure (PtBPC–MHN) intermediates described herein were formed preferentially over solitary salt precipitates as K_2PtCl_4 was allowed to saturate the AT-MNP surface with Pt^{2+} ions before adding NH_2OH to initiate polymerization. The PtBPC–MHNs were then isolated before performing a reduction step to form Pt–MHNs (Scheme 1, step 2).[29,30] Different reduction strategies were tested, including chemical reduction by sodium borohydride ($NaBH_4$) and thermal reduction on carbon support.

Characterization of PtBPC–MHN intermediates

Pt^{2+} adsorption to Fe_3O_4 nanoparticles was controlled by altering the concentration of K_2PtCl_4 reagent. Separate syntheses were carried with varied K_2PtCl_4 starting concentrations: 0.125 mM, 0.250 mM, 0.375 mM, and 0.500 mM. The resulting Pt/Fe atomic ratio was proportional to the K_2PtCl_4 concentration, as analyzed by flame atomic absorption (FAA) spectroscopy (Fig. S1, ESI†). Analysis by energy dispersive X-ray spectroscopy in conjunction with scanning transmission electron microscopy (STEM/EDX) led to good agreement with FAA, indicating that Pt is uniformly distributed throughout the sample (Fig. S1, ESI†). As a control, the synthesis was repeated with the exclusion of NH_2OH reagent. No evidence of adsorbed Pt^{2+} was found by STEM/EDX of the product from the control procedure (Fig. S2, ESI†), indicating that NH_2OH is essential for PtBPC–MHN formation.

Powder X-ray diffraction (XRD) and X-ray photoelectron spectroscopy (XPS) were used to elucidate the PtBPC–MHN structure. Only the XRD pattern corresponding to Fe_3O_4 crystal facets is present (Fig. 1a), which indicates that the PtBPC layer

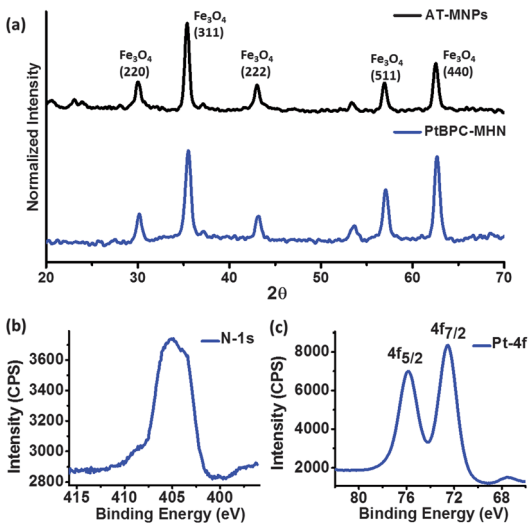

Fig. 1 (a) XRD patterns for AT-MNPs and PtBPC–MHNs, (b and c) XPS spectra of PtBPC–MHNs for (b) N-1s and (c) Pt-4f regions.

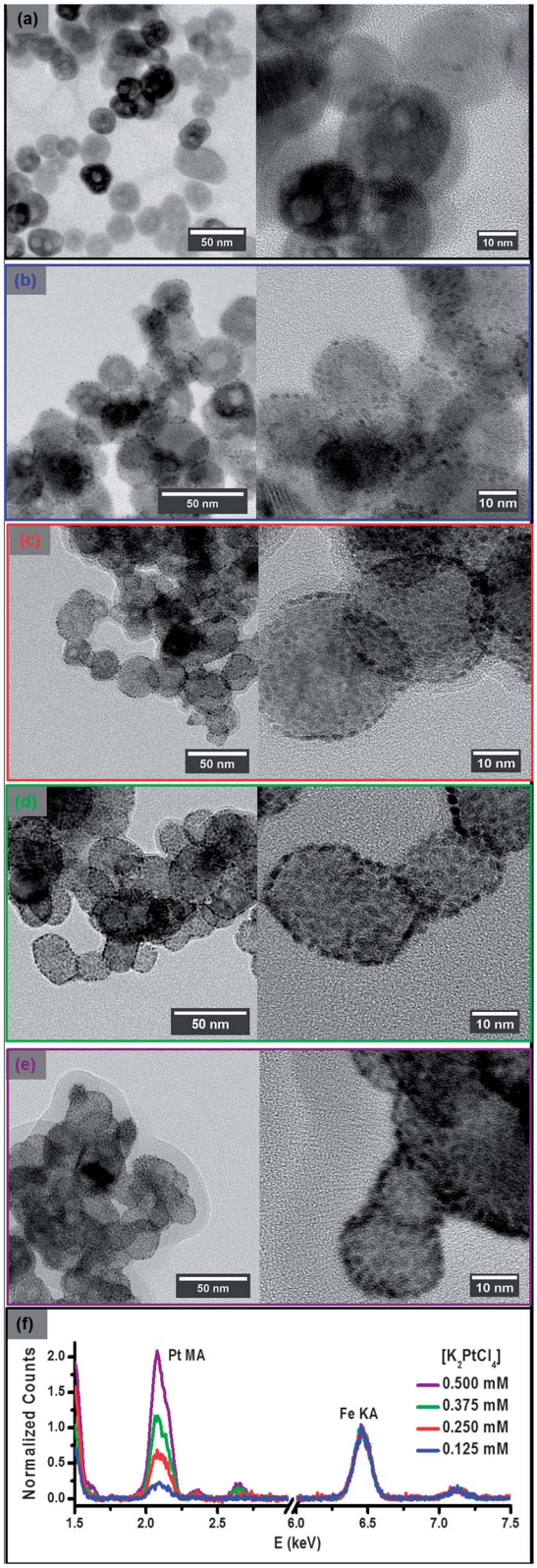

Fig. 2 (a) TEM of AT-MNPs, (b–e) TEM of Pt–MHNs formed immediately after e-beam triggered reduction of PtBPC–MHNs previously synthesized in the presence of (b) 0.125 mM, (c) 0.250 mM, (d) 0.375 mM, and (e) 0.500 mM K_2PtCl_4 and (f) corresponding EDX spectra for each Pt–MHN species, spectra normalized by Fe Kα peak maximum.

of the MHN is primarily amorphous. The Pt-4f XPS spectrum for the PtBPC–MHN intermediate is in the range corresponding to Pt^{2+} states[31] (Fig. 1c). The comparison of the N-1s and Pt-4f peak areas shown in Fig. 1b and c (adjusted by their relative sensitivity factors: 0.499 and 6.08, respectively) results in a N : Pt atomic ratio of 2.01 : 1, in excellent agreement with the expected ratio of 4 : 2 for the stoichiometry of $[Pt(NH_2OH)_4][PtCl_4]$.

Reduction by TEM beam

PtBPC–MHNs were observed to form ~2 nm size Pt domains during transmission electron microscopy (TEM) imaging due to the reducing power of the electron beam. Shown in Fig. 2 are the AT-MNP precursors and the resulting Pt–MHNs. All Pt nanocrystals were observed to be exclusively bound to Fe_3O_4 nanoparticle surfaces. EDX analysis confirms that Pt loading is proportional to the concentration of Pt ion precursor as relative Pt peak intensity increases with respect to the Fe peak (Fig. 2f).

Interplanar lattice spacing for both Pt (111) and Fe_3O_4 (311) were observed by high resolution TEM (Fig. 3). The observation of Pt (111) facets indicates that the platinum atoms are no longer part of a Pt^{2+} complex intermediate, but were completely reduced by the high intensity electron beam to Pt^0 nanoparticles.

Wet chemical reduction method

Pt–MHNs were also synthesized by chemical reduction of PtBPC–MHNs using $NaBH_4$ as the reducing agent in the presence of citrate stabilizer in aqueous media. Shown by scanning transmission electron microscopy (STEM) in Fig. 4, the resulting Pt–MHN product consists of polydispersed dendritic Pt nanostructures with larger domains than those observed after E-beam reduction. The Pt is not tightly packed or evenly deposited over the Fe_3O_4 surfaces so the underlying morphology of the Fe_3O_4 nanocrystal precursors is hardly recognizable. Some Fe_3O_4 particles have a higher percentage of exposed surface rather than Pt-covered. This is in contrast to the uniformly distributed Pt nanoparticle monolayers observed for Pt–MHNs formed under the electron beam.

The Pt-$4f_{7/2}$ binding energy (70.8 eV) is shifted 0.4 eV lower than the reference value for bulk Pt (71.2 eV).[31] This 0.4 eV decrease in binding energy has been previously reported for other Fe_3O_4–Pt nanocomposites and is attributed to charge transfer between the Fe_3O_4 and Pt domains.[3k,32] The Fe_3O_4 domain polarizes the nanocomposite and enriches the Pt domain with negative charge. This polarization effect is further supported by the work function difference[33] between Fe_3O_4(111) at 5.52 eV (ref. 34) and Pt(111) at 5.93 eV (ref. 35), which is equivalent to the observed spectral shift in binding energy (~0.4 eV).

Thermally driven reduction under ambient atmosphere

A thermal treatment method was applied to effectively control the growth of Pt on the Fe_3O_4 surface. PtBPC–MHNs were loaded onto carbon black supports and heated under ambient atmosphere at two different temperatures, 190 °C and 240 °C. A

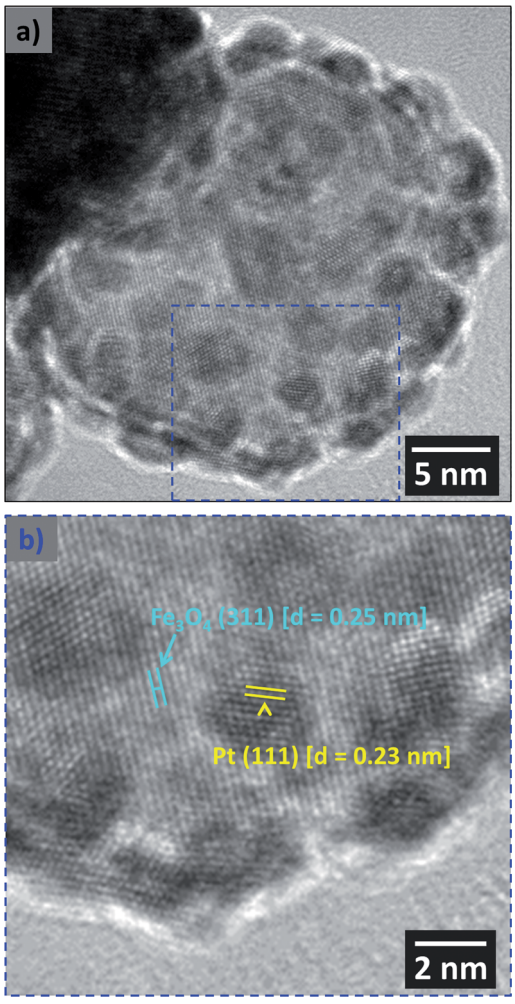

Fig. 3 High resolution TEM of (a) one Pt–MHN formed after electron beam induced reduction of PtBCP–MHNs and (b) blown up image of section outlined in blue. Interplanar lattice spacings are labeled for both Fe_3O_4 and Pt.

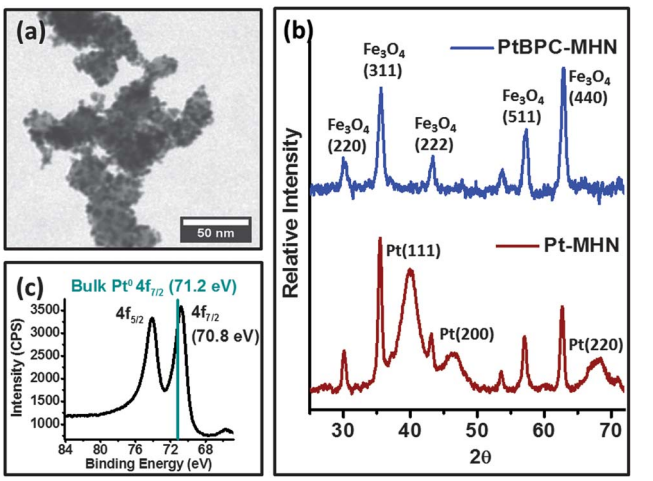

Fig. 4 Characterization of Pt–MHNs synthesized by wet chemical reduction of PtBPC–MHNs from 0.375 mM K_2PtCl_4 synthesis: (a) bright field STEM of Pt–MHN, (b) XRD patterns for PtBPC–MHN precursor and Pt–MHN, and (c) XPS Pt-4f spectrum for Pt–MHN. Pt-$4f_{7/2}$ peak position of bulk Pt^0 is marked for reference.

third Pt–MHN product was prepared by reacting the 240 °C-treated sample with $NaBH_4$ in solution. As shown in Fig. 4, Pt–MHNs were mostly found as aggregates partially adhered to the carbon support due to their strong ferrimagnetic interparticle attractions[36] and hydrophilicity. However, the final Pt–MHN product is composed of Fe_3O_4 core particles with high Pt surface coverage, in contrast to the Pt–MHNs resulted from $NaBH_4$ reduction alone. For further structural characterization, EDX line scan and area map profiles were performed on a single Pt–MHN (Fig. 5b–e). The EDX profiles show that Fe signal is more concentrated toward the core of the particle while X-ray emissions corresponding to Pt originate from the outer region, confirming a Fe_3O_4@Pt core@shell-type structure.

Structural interrogation of carbon supported Pt–MHN products (Pt–MHN/Cs) was performed using powder XRD (Fig. 6a). XRD of the Pt–MHN/C after 190 °C baking in air shows some weak Pt diffraction band intensity while the sample treated at 240 °C shows more intense Pt signal with respect to Fe_3O_4, signifying the increased reduction of Pt and formation of Pt nanoparticles with increasing temperature. The XRD pattern of 240 °C-annealed Pt–MHN/C after $NaBH_4$ reduction treatment is rich with broad Pt diffraction peaks, indicating that it is the most developed Pt–MHN/C of those analyzed with respect to Pt^0 content.

Pt-4f XPS data further supports the trend of thermally driven Pt reduction on the Fe_3O_4 nanocrystalline surfaces (Fig. 6b), as

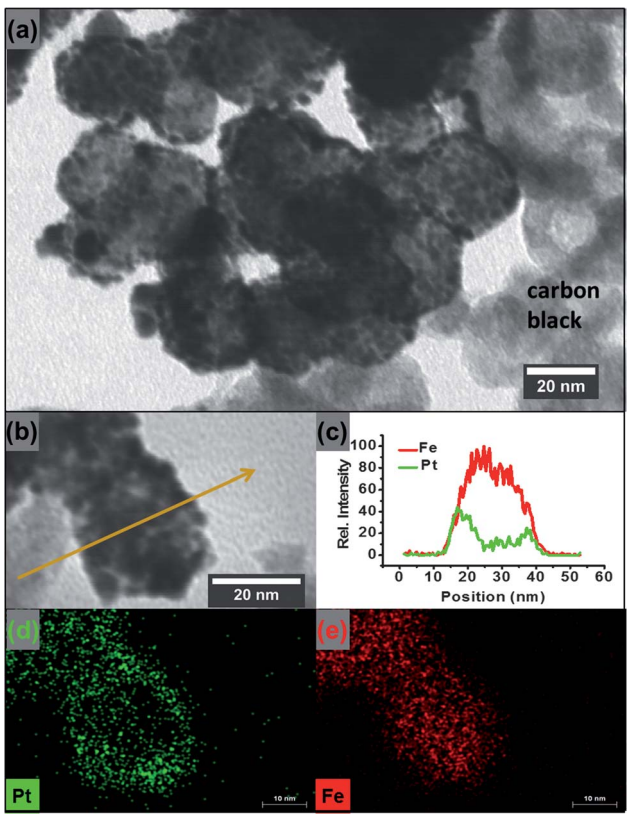

Fig. 5 STEM/EDX characterization of Pt–MHN/C: (a) STEM image of Pt–MHN aggregates on carbon support after 240 °C thermal treatment and chemical reduction by $NaBH_4$. (b) High magnification of single Pt–MHN with corresponding (c) EDX line profile and (d and e) Pt/Fe EDX mapping.

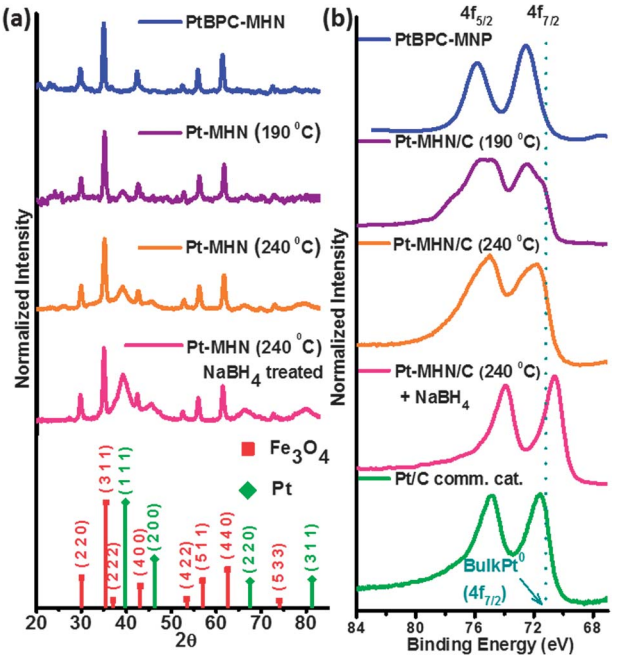

Fig. 6 Characterization of Pt–MHNs synthesized by different methods: (a) XRD patterns for PtBPC–MHNs, Pt–MHN/Cs formed by thermal treatment in air at 190 °C and 240 °C, and fully reduced Pt–MHN/C formed after wet chemical reduction of the 240 °C-treated species by $NaBH_4$. Fe_3O_4 and Pt XRD line patterns with Miller index labels are included for reference. (b) XPS Pt-4f spectra for PtBPC–MHN, Pt–MHN/C species, and Pt/C commercial catalyst. Pt-$4f_{7/2}$ binding energy of bulk Pt^0 is marked for reference.

new shoulders appear at lower binding energy for the heat treated samples. The peaks/shoulders at more positive binding energies correspond to oxidized Pt^{2+}–BPCs, while those at lower binding energies refer to reduced Pt nanoparticles formed on the Fe_3O_4 surface. The deconvoluted spectra are provided in Fig. S3 of ESI,† indicating the multiple Pt chemical states incorporated in the thermally treated samples. The relative intensity of peaks at lower binding energy is higher for the sample baked at 240 °C *vs.* the one treated at 190 °C, indicating that thermal treatment at higher temperature leads to more Pt reduction. After reacting the 240 °C-annealed sample with $NaBH_4$, the resulting Pt-4f peak shapes are sharper and shifted more negative than those of the Pt/C reference, representing a fully reduced Pt–MHN species.

The Pt-$4f_{7/2}$ maximum for the final Pt–MHN/C product (pink curve) is positioned at 70.6 eV, which is ~0.6 eV lower in binding energy than metallic platinum. The magnitude of this shift in binding energy is 0.2 eV larger than that observed for the sample described earlier (Fig. 4c) along with previously reported hybrid Pt–Fe_3O_4 nanostructures.[3k,32]

The cause of the increased shifting in binding energy can be rationalized by applying the same principles used to describe charge transfer at the well-studied metal–semiconductor interface.[2c] The work of Verykios and Ioannides,[37] in specific, provides a theoretical analysis to a somewhat analogous system modeled after spherical Pt nanoparticles halfway embedded into a TiO_2 semiconductor support. The authors' theoretical

approach established a Pt nanoparticle size dependence in relation to the number of electrons transferred per Pt atom at the interface; *i.e.* the smaller the size of the Pt nanoparticle, the greater the magnitude of charge transfer.[37] A similar dependence may be responsible for the deviation in electronic properties observed among different Pt–MHN species. Upon comparison to the Pt–MHNs formed by chemical reduction alone (Fig. 4) and the 5 nm diameter Pt nanoparticles of Pt–Fe_3O_4 heterodimers[3k,32a] (Fig. S7, ESI†), the Pt nanodomains shown in Fig. 5 are much smaller in terms of average thickness between the Pt–Fe_3O_4 interface and outer exposed Pt surface. This confinement results in a relatively higher magnitude of charge transfer, which leads to further downshifting of the Pt-4f core electron binding energy.

The mechanism for thermally driven reduction of PtBPC–MHNs is unclear, since many possible redox reactions could take place between the Pt(II) complex species and potential reducing agents. Such reactions may involve reduction of the Pt^{2+} by coordinating NH_2OH ligands[24,38] and/or the Fe_3O_4 surface itself, which in turn may oxidize to Fe_2O_3. The standard reduction potentials for the $PtCl_4^{2-}$/Pt(s) and $3Fe_2O_3$(s)/$2Fe_3O_4$(s) reactions are 0.755 V (ref. 39) and 0.66 V (ref. 40) *vs.* NHE, respectively, giving a net redox potential of *ca.* +0.10 V for the reaction described by eqn (1). Despite this positive value, the reaction does not spontaneously occur in step 1 during the 60 °C synthesis of the PtBPC–MHN intermediate due to Fe_3O_4 surface stabilization by the 1,6-hexanediamine ligands. This stabilization may be compromised at more elevated temperatures, allowing the reaction to proceed.

$$PtCl_4^{2-} + 2Fe_3O_4(s) + H_2O \rightarrow Pt(s) + 3Fe_2O_3(s) + 2H^+ + 4Cl^- \quad (1)$$

The XRD results do not suggest that any substantial amount of Fe_3O_4 oxidation occurs during the thermal treatment (Fig. 6a). But powder XRD is not sensitive enough to detect only a few surface layers of Fe_2O_3, so reaction 1 cannot be ruled out. A Pt(II) complex may also disproportionate to Pt(IV) species and metallic Pt. For example, tetrachloroplatinate ion disproportionates to hexachloroplatinate and metallic platinum according to eqn (2).

$$2[PtCl_4^{2-}] \rightarrow [PtCl_6^{2-}] + Pt(s) + 2Cl^- \quad (2)$$

Any of these three processes (reduction by amine ligands, Fe_3O_4 surface reaction, or disproportionation) could contribute to the reduction of the PtBPC–MHNs.

While the thermal treatment only achieved partial reduction of the total Pt content, it did successfully promote Pt nanoparticle nucleation and growth at the Fe_3O_4 surface. Pt(0) atoms that are resulted upon chemical reduction by $NaBH_4$ then supplement these nucleation sites, thus growing larger Pt nanodomains (Fig. 5a). In contrast, the mechanism of nucleation for the previous Pt–MHN sample formed solely by $NaBH_4$ reduction is quite different, since many Pt nanoparticles spontaneously nucleate upon fast reduction without epitaxial interfacial attachment to Fe_3O_4, leading to the more disordered Pt–MHNs (Fig. 4a).

Electrocatalytic evaluation of Pt–MNCs

The catalytic activity of Pt–MHNs for ORR was studied by rotating disk voltammetry in O_2-saturated 0.10 M KOH, using glassy carbon working electrodes coated with thin films of Pt–MHN/C catalysts. The rotating disk linear sweep voltammograms (LSVs) of Pt–MHNs and their precursors are presented in Fig. S4, ESI.† The poor catalytic activity of the divalent PtBCP–MHN/C species is almost identical to that of the nonplatinized AT-MNP/C, which is expected since the platinum is bound to the Fe_3O_4 core particles as stable Pt^{2+} complexes. After the 240 °C treatment in air, the Pt–MHN/C improves in electrocatalytic activity, but the onset potential is still relatively too far negative and the mass transfer limited current density (j_l) remains far below what is expected for completing the net four-electron reduction,[41] according to the Levich equation:[23,42]

$$j_l = 0.62nFD^{2/3}\omega^{1/2}\nu^{-1/6}C \quad (3)$$

where n is the number of electrons transferred, F is the Faraday constant, D is the diffusion coefficient for dissolved O_2 (1.9×10^{-5} cm^2 s^{-1}),[43] ω is rotation rate (1600 rpm or 167.7 rad s^{-1}), ν is the kinematic viscosity (0.01 cm^2 s^{-1}), and C is the saturated O_2 concentration in 0.10 M KOH (1.2×10^{-6} mol cm^{-3}).[21,44] The ORR activity for Pt–MHN/Cs that were synthesized by chemical reduction is notably higher than that for Pt–MHN/Cs that were only treated thermally in air. The final Pt–MHN/C product resulting from both thermal and subsequent $NaBH_4$ reduction is the most active catalyst for ORR, having the most positively-shifted onset potential and highest limiting current density.

An RDE experiment was also performed on a commercial Pt/C fuel cell catalyst for direct comparison of electrocatalytic ORR activity to that of Pt–MHN/C. As shown in Fig. 7a, both catalysts generate the same mass transfer limited current density. The j_l value was used to calculate a value of 3.8 for n by eqn (3). This suggests that both catalysts efficiently promote complete 4 electron reduction of oxygen according to eqn (4).

$$O_2 + 2H_2O + 4e^- \rightarrow 4OH^- \quad (4)$$

The kinetic currents at 0.85 V *vs.* RHE were calculated according to the Koutecky–Levich equation;[23] then normalized by the electrochemically active Pt surface area (ECSA) and Pt mass loading for specific activity (Fig. 7b) and mass activity (Fig. 7c), respectively. The Pt ECSA was calculated from the overall charge associated with hydride desorption determined by cyclic voltammetry in 0.10 M $HClO_4$ (Fig. S5, ESI†). Pt mass loading was calculated based on thermogravimetric analysis (TGA) (Fig. S6, ESI†) of Pt–MHN/C in combination with the %Pt composition results from FAA. As shown in Fig. 7b, the Pt–MHN/C catalyst is about two times more active than the Pt/C commercial catalyst in terms of specific activity.

In contrast to specific activity, the mass activity of Pt–MHN/C is lower than the Pt/C catalyst (Fig. 7c). This is due to the aggregation of Pt–MHNs observed by STEM (Fig. 5a). The interaction between hydrophilic PtBCP–MHNs and the relatively hydrophobic carbon support particles is weaker than interparticle interactions that PtBCP–MHNs have with one another; therefore

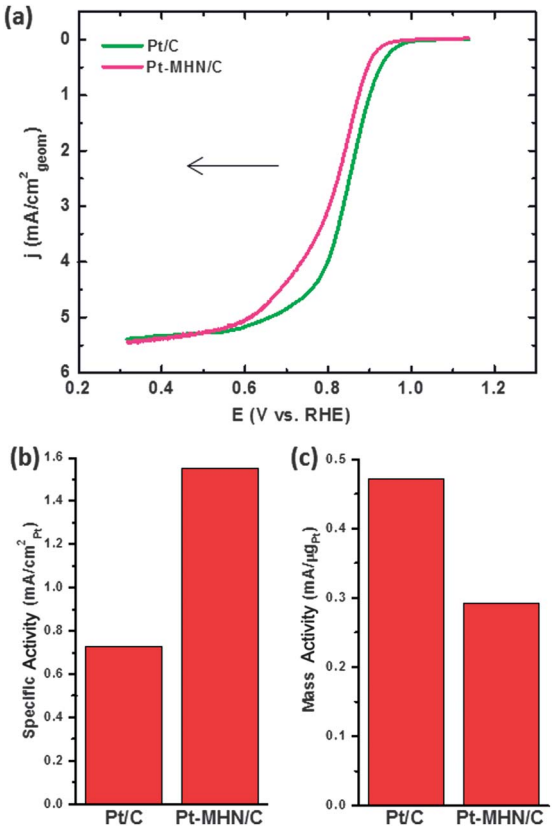

Fig. 7 (a) Rotating disk voltammograms (cathodic scan, 1600 rpm, 5 mV s^{-1}), (b) Pt specific activity, and (c) Pt mass activity for ORR by Pt–MHN/C and Pt/C commercial catalysts at 0.85 V *vs.* RHE. The kinetic current values calculated from the data in (a) were normalized by the Pt ECSA and mass loading for specific and mass activity, respectively.

large PtBCP–MHN aggregates are formed. During thermal and chemical reduction treatments, the developing Pt nanoparticles of one Pt–MHN sinter with those of neighboring Fe_3O_4 cores, forming large aggregates and leaving much of the Pt surfaces buried. Also shown in Fig. 5a is the relatively low amount of contact sites between the catalyst and the conductive carbon support. Both low conductivity and buried Pt surfaces are most likely responsible for the relatively low mass activity and low ECSA (Fig. S5, ESI†). The commercial Pt/C catalyst ECSA is about 4 times higher than that of the Pt–MHN/C catalyst film, which in turn accounts for the ~25 mV negative shift in ORR onset potential from that of the Pt/C catalyst.[45]

Charge transfer between the Fe_3O_4 and Pt domains is primarily responsible for the enhancement in ORR activity. Similar ligand effects have been reported for many other hybrid metal-on-metal oxide systems.[3b,c,h,i,8e,f,9,11] Pt nanoparticles on Fe_3O_4 supports are more electron-rich than isolated Pt,[3k,32a] as evidenced by XPS spectroscopy (Fig. 6b). One might consider such electronic enrichment to be harmful for ORR since d-electron vacancies on Pt promote adsorption of O_2.[46] While it is important that the binding of O_2 and intermediates be sufficiently strong to promote charge transfer and O–O bond cleavage, a Pt surface that binds oxygen too tightly is also more susceptible to the blocking effect, whereby spectator oxygenated adsorbates prevent O_2 from adsorbing on catalytic Pt sites.[47] Therefore, it is desirable to slightly reduce the oxygen binding energy to increase availability of Pt surface sites and achieve higher ORR activity.

The catalytic stability of Pt–MHN/C was also evaluated by an electrochemical method. Chronoamperometric analysis was performed on the catalyst films by applying a potential step of 0.85 V in O_2-saturated 0.10 M KOH and monitoring the relative change in catalytic current over time (Fig. 8). The electrocatalytic current for the Pt/C commercial catalyst and Pt–MHN/C remains constant over the span of 9000 seconds. The stability of 5–17 nm Pt–Fe_3O_4 heterodimers supported on carbon black (Pt–MHD/C) was also tested for comparison (see Fig. S6 of ESI† for STEM characterization of Pt–MHDs). As shown in Fig. 8, the Pt–MHD/C catalyst deactivates over time. This occurs because the Pt domain of Pt–MHDs does not protect Fe_3O_4 from oxidation and/or dissolution, thus the synergetic enhancement of electrocatalytic activity provided from Fe_3O_4 decreases as the material degrades. This is not the case for Pt–MHNs, because the high surface coverage of Pt serves to protect the Fe_3O_4 core domains.

Further stabilization against Pt deactivation may be imparted by the Fe_3O_4. Pt nanoparticles deposited solely on amorphous carbon lose their activity over time in acidic/alkaline environments due to corrosion of the support, which leads to sintering and/or diffusion of the Pt nanoparticles.[48] Oxide supports have been shown to help fortify Pt catalysts against such deactivation processes, since Pt nanoparticles are firmly anchored to the oxide surface.[3i,49] Exceptional stability is conferred to the Pt–MHNs, owing to the strength of Pt–Fe_3O_4 metal–support interactions.[12,33]

Synthesis and characterization of Pt–SiHMs

The application of the Pt coating procedure is not limited to Fe_3O_4 nanoparticle surfaces since any amine-functionalized surface can serve as nucleation sites for PtBPC growth. As proof of this concept, we selected amine-terminated silica microspheres to serve as host substrates in place of AT-MNPs, thus forming hybrid microstructures of SiO_2 and PtBPC, followed by $NaBH_4$ reduction to form Pt–SiO_2 hybrid microstructures (Pt–SiHMs).

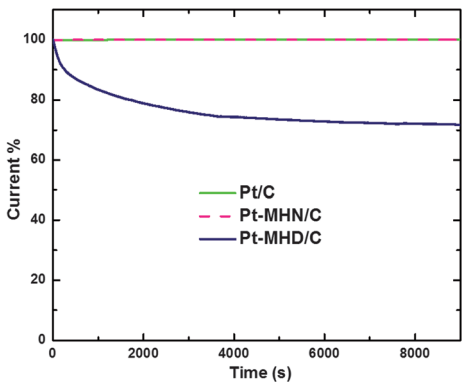

Fig. 8 Stability tests for Pt/C, Pt–MHN/C and Pt–MHD/C catalysts; current% *vs.* time for a potential step of 0.85 V *vs.* RHE and rotation rate of 200 rpm. All scans are for O_2 sat. 0.10 M KOH.

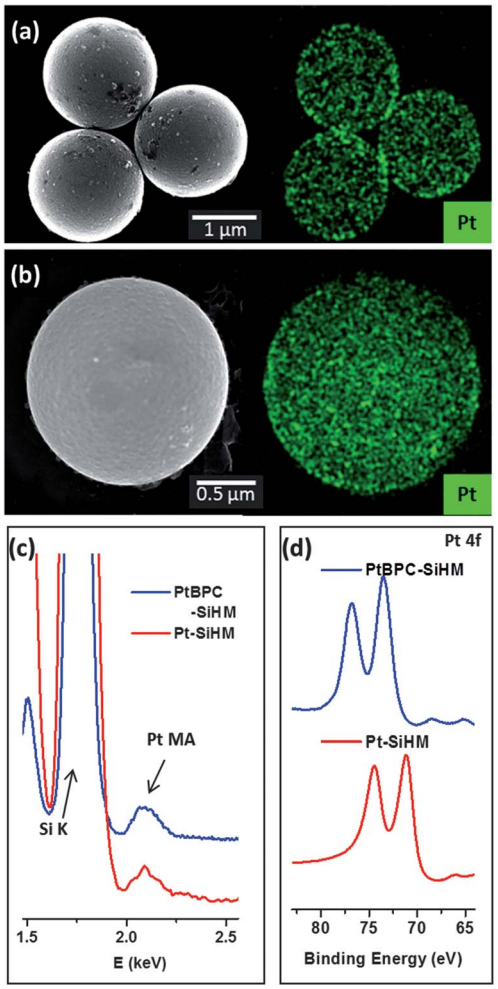

Fig. 9 STEM/EDX mapping of Pt on (a) PtBPC–SiHMs and (b) Pt–SiHMs. (c) EDX and (d) XPS spectra (Pt-4f) for PtBPC–SiHMs and Pt–SiHMs.

STEM/EDX mapping reveals that a very thin layer of Pt adsorbs to the surface of the SiO_2 microbeads following the first and second steps of the synthesis (Fig. 9a–c). The Pt-4f XPS spectrum for the first step is similar to that observed for PtBPC–MHNs, indicating a similar Pt^{2+} complex structure (Fig. 9). The spectrum of the reduced Pt–SiHM species is not shifted as negative as that of Pt–MHN (Fig. 4c), since the SiO_2 does not electronically enrich the Pt shell as in the case of Pt–MHNs.

Conclusions

In this work we have introduced two new types of Pt–Fe_3O_4 nanohybrid structures. One structure is comprised of a linear system of complexed Pt^{2+} species adsorbed to the Fe_3O_4 nanocrystal surface. The controlled reduction of this hybrid results in the high-density coating of the Fe_3O_4 nanodomains with a semicontinuous layer of ~2–3 nm Pt. The latter Pt–Fe_3O_4 hybrid was found to exhibit charge transfer from the Fe_3O_4 to the Pt domains, as evidenced by the shifting of Pt core electrons to lower binding energy. This electronic enrichment of Pt served to enhance Pt surface activity for the electroreduction of oxygen, resulting in a two-fold increase of specific activity with respect to commercial Pt nanocatalysts. The Pt–MHNs are also shown to be more stable ORR catalysts than Pt–Fe_3O_4 heterodimers.

In light of our findings with Fe_3O_4 and SiO_2 substrates, we propose that the electroless Pt deposition method described in this paper can be generally applied to virtually any amine-functionalized surface. The versatility of this approach is significant for the fuel cell catalysis community, as it can be adopted as a general strategy to control Pt deposition over a great range of catalyst support materials. Moreover, we predict that similar procedures can be developed for the design of Pd–MHNs, since the linear coordination chemistry of Pd^{2+} is quite similar to Pt^{2+} (*e.g.* Vauquelin's salt).[50] The Pt–MHNs must be supported on a conductive material such as carbon black to be active, due to the low conductivity of Fe_3O_4. Pt–MHNs with higher colloidal stability would be more likely to be uniformly distributed throughout the chosen conductive support. We propose that the mass activity can be improved by applying smaller, superparamagnetic Fe_3O_4 cores instead of the larger, ferrimagnetic particles used in this study, since interparticle magnetic attraction drives their aggregation.[36]

Our efforts are currently focused on modifying the synthetic methods to achieve water-dispersible and colloidally stable Pt–MHNs for target applications that exploit their superparamagnetic/electrocatalytic bifunctionality. With the help of our collaborators, we are currently pursuing the application of Pt–MHNs towards improving the detection limits of ultrasensitive DNA sensors based on electrocatalytic amplification[51] of individual DNA hybridization events.[51h,i]

Acknowledgements

We thank the Defense Threat Reduction Agency (DTRA) (Grant HDTRA1-11-1-0005) for financial support. D. R. acknowledges Nellymar Membreno for acquiring TEM images, Matthew Charlton for assistance with XPS, and Dr Anthony Dylla for acquiring TGA data. D. R. also thanks Dr Radhika Dasari, Jacob Goran, and William Hardin for helpful discussions.

Notes and references

1 (*a*) R. Costi, A. E. Saunders and U. Banin, *Angew. Chem., Int. Ed.*, 2010, **49**, 4878; (*b*) P. D. Cozzoli, T. Pellegrino and L. Manna, *Chem. Soc. Rev.*, 2006, **35**, 1195; (*c*) C. Wang, C. Xu, H. Zeng and S. Sun, *Adv. Mater.*, 2009, **21**, 3045.

2 (*a*) S. Surnev, A. Fortunelli and F. P. Netzer, *Chem. Rev.*, 2012, **113**, 4314; (*b*) Q. Fu, F. Yang and X. Bao, *Acc. Chem. Res.*, 2013, **46**, 1692; (*c*) Q. Fu and T. Wagner, *Surf. Sci. Rep.*, 2007, **62**, 431.

3 (*a*) A. G. Dylla and K. J. Stevenson, *Chem. Commun.*, 2011, **47**, 12104; (*b*) B. Y. Xia, B. Wang, H. B. Wu, Z. Liu, X. Wang and X. W. Lou, *J. Mater. Chem.*, 2012, **22**, 16499; (*c*) Y. Fan, Z. Yang, P. Huang, X. Zhang and Y.-M. Liu, *Electrochim. Acta*, 2013, **105**, 157; (*d*) M. C. Orilall, F. Matsumoto, Q. Zhou, H. Sai, H. c. D. Abruña, F. J. DiSalvo and U. Wiesner, *J. Am. Chem. Soc.*, 2009, **131**, 9389; (*e*) K. Sasaki, L. Zhang and R. R. Adzic, *Phys. Chem. Chem. Phys.*, 2008, **10**, 159; (*f*) J. Rajeswari, B. Viswanathan and

T. K. Varadarajan, *Mater. Chem. Phys.*, 2007, **106**, 168; (*g*) T. Maiyalagan and B. Viswanathan, *J. Power Sources*, 2008, **175**, 789; (*h*) D. A. Slanac, A. Lie, J. A. Paulson, K. J. Stevenson and K. P. Johnston, *J. Phys. Chem. C*, 2012, **116**, 11032; (*i*) K. W. Kim, S. M. Kim, S. Choi, J. Kim and I. S. Lee, *ACS Nano*, 2012, **6**, 5122; (*j*) S. Palchoudhury, Y. Xu, J. Goodwin and Y. Bao, *J. Mater. Chem.*, 2011, **21**, 3966; (*k*) C. Wang, H. Daimon and S. Sun, *Nano Lett.*, 2009, **9**, 1493.

4 (*a*) S. J. Tauster, S. C. Fung and R. L. Garten, *J. Am. Chem. Soc.*, 1978, **100**, 170; (*b*) S. J. Tauster, *Acc. Chem. Res.*, 1987, **20**, 389; (*c*) S. J. Tauster, S. C. Fung, R. T. K. Baker and J. A. Horsley, *Science*, 1981, **211**, 1121.

5 Y.-J. Gu and W.-T. Wong, *J. Electrochem. Soc.*, 2006, **153**, A1714.

6 H.-P. Zhou, H.-S. Wu, J. Shen, A.-X. Yin, L.-D. Sun and C.-H. Yan, *J. Am. Chem. Soc.*, 2010, **132**, 4998.

7 (*a*) Z. Miao, H. Yu, W. Song, L. Hao, Z. Shao, Q. Shen, J. Hou and B. Yi, *Int. J. Hydrogen Energy*, 2010, **35**, 5552; (*b*) N. Travitsky, T. Ripenbein, D. Golodnitsky, Y. Rosenberg, L. Burshtein and E. Peled, *J. Power Sources*, 2006, **161**, 782.

8 (*a*) S. G. Neophytides, K. Murase, S. Zafeiratos, G. Papakonstantinou, F. E. Paloukis, N. V. Krstajic and M. M. Jaksic, *J. Phys. Chem. B*, 2006, **110**, 3030; (*b*) G. R. Dieckmann and S. H. Langer, *Electrochim. Acta*, 1998, **44**, 437; (*c*) L. Xiong and A. Manthiram, *Electrochim. Acta*, 2004, **49**, 4163; (*d*) L. M. Vračar, N. V. Krstajić, V. R. Radmilović and M. M. Jakšić, *J. Electroanal. Chem.*, 2006, **587**, 99; (*e*) N. Rajalakshmi, N. Lakshmi and K. S. Dhathathreyan, *Int. J. Hydrogen Energy*, 2008, **33**, 7521; (*f*) H. Chhina, S. Campbell and O. Kesler, *J. Electrochem. Soc.*, 2009, **156**, B1232.

9 L. Zhang, L. Wang, C. M. B. Holt, T. Navessin, K. Malek, M. H. Eikerling and D. Mitlin, *J. Phys. Chem. C*, 2010, **114**, 16463.

10 O. Savadogo and P. Beck, *J. Electrochem. Soc.*, 1996, **143**, 3842.

11 Y.-P. Xiao, W.-J. Jiang, S. Wan, X. Zhang, J.-S. Hu, Z.-D. Wei and L.-J. Wan, *J. Mater. Chem. A*, 2013, **1**, 7463.

12 R. Wang, J. Jia, H. Wang, Q. Wang, S. Ji and Z. Tian, *J. Solid State Electrochem.*, 2013, **17**, 1021.

13 (*a*) U. Colombo, G. Fagherazzi, F. Gazzarrini, G. Lanzavecchia and G. Sironi, *Nature*, 1964, **202**, 175; (*b*) U. Colombo, F. Gazzarrini, G. Lanzavecchia and G. Sironi, *Science*, 1965, **147**, 1033; (*c*) K. J. Gallagher, W. Feitknecht and U. Mannweiler, *Nature*, 1968, **217**, 1118; (*d*) U. Colombo, G. Fagherazzi, F. Gazzarrini, G. Lanzavecchia and G. Sironi, *Nature*, 1968, **219**, 1036.

14 S. Haruyama and K. Masamura, *Corros. Sci.*, 1978, **18**, 263.

15 (*a*) P. Tremaine and J. LeBlanc, *J. Solution Chem.*, 1980, **9**, 415; (*b*) S. E. Ziemniak, M. E. Jones and K. E. S. Combs, *J. Solution Chem.*, 1995, **24**, 837.

16 J. Tang, M. Myers, K. A. Bosnick and L. E. Brus, *J. Phys. Chem. B*, 2003, **107**, 7501.

17 D. Li, C. Wang, D. Tripkovic, S. Sun, N. M. Markovic and V. R. Stamenkovic, *ACS Catal.*, 2012, **2**, 1358.

18 L. Wang, J. Bao, L. Wang, F. Zhang and Y. Li, *Chem.–Eur. J.*, 2006, **12**, 6341.

19 C. Wang, H. Daimon, T. Onodera, T. Koda and S. Sun, *Angew. Chem., Int. Ed.*, 2008, **47**, 3588.

20 (*a*) D. C. Lee, F. V. Mikulec, J. M. Pelaez, B. Koo and B. A. Korgel, *J. Phys. Chem. B*, 2006, **110**, 11160; (*b*) M. R. Rasch, K. V. Sokolov and B. A. Korgel, *Langmuir*, 2009, **25**, 11777.

21 D. A. Slanac, W. G. Hardin, K. P. Johnston and K. J. Stevenson, *J. Am. Chem. Soc.*, 2012, **134**, 9812.

22 J. M. Doña Rodríguez, J. A. Herrera Melián and J. Pérez Peña, *J. Chem. Educ.*, 2000, **77**, 1195.

23 A. J. Bard and L. R. Faulkner, *Electrochemical Methods: Fundamentals and Applications*, Wiley, 2000.

24 J. L. Lyon, D. A. Fleming, M. B. Stone, P. Schiffer and M. E. Williams, *Nano Lett.*, 2004, **4**, 719.

25 G. Magnus, *Ann. Phys.*, 1828, **14**, 239.

26 W. Caseri, *Platinum Met. Rev.*, 2004, **48**, 91.

27 M. Atoji, J. W. Richardson and R. E. Rundle, *J. Am. Chem. Soc.*, 1957, **79**, 3017.

28 L. A. Tschugaev and I. I. Tschernjaev, *J. Chem. Soc., Trans.*, 1918, **113**, 884.

29 Magnus's salts have previously been shown to be excellent precursors for the shape-selective synthesis of Pt nanoparticles.

30 W. Zhu, A.-X. Yin, Y.-W. Zhang and C.-H. Yan, *Chem.–Eur. J.*, 2012, **18**, 12222.

31 C. D. Wagner and G. E. Muilenberg, *Handbook of X-ray photoelectron spectroscopy: a reference book of standard data for use in X-ray photoelectron spectroscopy*, Physical Electronics Division, Perkin-Elmer Corp., 1979.

32 (*a*) M. R. Buck, J. F. Bondi and R. E. Schaak, *Nat. Chem.*, 2012, **4**, 37; (*b*) S. Kumari and R. P. Singh, *Int. J. Biol. Macromol.*, 2012, **51**, 76.

33 Z. H. Qin, M. Lewandowski, Y. N. Sun, S. Shaikhutdinov and H. J. Freund, *J. Phys. Chem. C*, 2008, **112**, 10209.

34 W. Weiss and W. Ranke, *Prog. Surf. Sci.*, 2002, **70**, 1.

35 W. M. Haynes, D. R. Lide and T. J. Bruno, *CRC Handbook of Chemistry and Physics 2012–2013*, CRC Press, 2012.

36 N. Lee, H. Kim, S. H. Choi, M. Park, D. Kim, H.-C. Kim, Y. Choi, S. Lin, B. H. Kim, H. S. Jung, H. Kim, K. S. Park, W. K. Moon and T. Hyeon, *Proc. Natl. Acad. Sci. U. S. A.*, 2011, **108**, 2662.

37 T. Ioannides and X. E. Verykios, *J. Catal.*, 1996, **161**, 560.

38 K. R. Brown and M. J. Natan, *Langmuir*, 1998, **14**, 726.

39 A. J. Bard, R. Parsons, J. Jordan and I. U. o. Pure and A. Chemistry, *Standard Potentials in Aqueous Solutions*, Taylor & Francis Group, 1985.

40 S. C. Pang, S. F. Chin and M. A. Anderson, *J. Colloid Interface Sci.*, 2007, **311**, 94.

41 J. Perez, E. R. Gonzalez and E. A. Ticianelli, *Electrochim. Acta*, 1998, **44**, 1329.

42 V. G. Levich, *Physicochemical hydrodynamics*, Prentice-Hall, Englewood Cliffs, N.J., 1962.

43 Z. Lin, G. Waller, Y. Liu, M. Liu and C.-P. Wong, *Adv. Energy Mater.*, 2012, **2**, 884.

44 G. Wiberg, K. Mayhofer and M. Arenz, *ECS Trans.*, 2009, **19**, 37.
45 B. Merzougui and S. Swathirajan, *J. Electrochem. Soc.*, 2006, **153**, A2220.
46 T. Toda, H. Igarashi, H. Uchida and M. Watanabe, *J. Electrochem. Soc.*, 1999, **146**, 3750.
47 (*a*) V. R. Stamenkovic, B. S. Mun, M. Arenz, K. J. J. Mayrhofer, C. A. Lucas, G. Wang, P. N. Ross and N. M. Markovic, *Nat. Mater.*, 2007, **6**, 241; (*b*) V. R. Stamenkovic, B. Fowler, B. S. Mun, G. Wang, P. N. Ross, C. A. Lucas and N. M. Marković, *Science*, 2007, **315**, 493.
48 (*a*) X. Wang, W. Li, Z. Chen, M. Waje and Y. Yan, *J. Power Sources*, 2006, **158**, 154; (*b*) L. Cademartiri and G. A. Ozin, *Adv. Mater.*, 2009, **21**, 1013; (*c*) A. Cao, R. Lu and G. Veser, *Phys. Chem. Chem. Phys.*, 2010, **12**, 13499; (*d*) B. Y. Xia, W. T. Ng, H. B. Wu, X. Wang and X. W. Lou, *Angew. Chem., Int. Ed.*, 2012, **51**, 7213; (*e*) B. Y. Xia, H. B. Wu, Y. Yan, X. W. Lou and X. Wang, *J. Am. Chem. Soc.*, 2013, **135**, 9480.
49 S.-Y. Huang, P. Ganesan, S. Park and B. N. Popov, *J. Am. Chem. Soc.*, 2009, **131**, 13898.
50 J. Bremi, D. Brovelli, W. Caseri, G. Hähner, P. Smith and T. Tervoort, *Chem. Mater.*, 1999, **11**, 977.
51 (*a*) X. Xiao, F.-R. F. Fan, J. Zhou and A. J. Bard, *J. Am. Chem. Soc.*, 2008, **130**, 16669; (*b*) X. Xiao, S. Pan, J. S. Jang, F.-R. F. Fan and A. J. Bard, *J. Phys. Chem. C*, 2009, **113**, 14978; (*c*) H. Zhou, F.-R. F. Fan and A. J. Bard, *J. Phys. Chem. Lett.*, 2010, **1**, 2671; (*d*) H. Zhou, J. H. Park, F.-R. F. Fan and A. J. Bard, *J. Am. Chem. Soc.*, 2012, **134**, 13212; (*e*) S. J. Kwon, F.-R. F. Fan and A. J. Bard, *J. Am. Chem. Soc.*, 2010, **132**, 13165; (*f*) S. J. Kwon and A. J. Bard, *J. Am. Chem. Soc.*, 2012, **134**, 7102; (*g*) R. Dasari, D. A. Robinson and K. J. Stevenson, *J. Am. Chem. Soc.*, 2012, **135**, 570; (*h*) S. J. Kwon and A. J. Bard, *J. Am. Chem. Soc.*, 2012, **134**, 10777; (*i*) T. M. Alligrant, E. G. Nettleton and R. M. Crooks, *Lab Chip*, 2013, **13**, 349.